Energy & Environmental Science

COMMUNICATION

View Article Online
View Journal

Cite this: DOI: 10.1039/c4ee02358g

Ultrathin self-powered artificial skin†

Tae Il Lee,‡[a] Woo Soon Jang,‡[b] Eungkyu Lee,[cd] Youn Sang Kim,[cd] Zhong Lin Wang,[e] Hong Koo Baik*[b] and Jae Min Myoung*[b]

Received 26th July 2014
Accepted 22nd September 2014

DOI: 10.1039/c4ee02358g

www.rsc.org/ees

Herein, we introduce an ultra-thin self-powered artificial skin (SPAS) based on a piezoelectric nanogenerator, which harvests stored elastic deformation energy produced by the bending and stretching actions of the skin. This finding is an important step toward building a self-powered "smart skin".

The skin of a living organism is filled with sensors designed to perceive various external physical or chemical stimuli and to maintain homeostasis by transferring this information to the brain.[1–4] Various artificial sensors that can detect changes in pressure, temperature, light, adsorbed chemicals, *etc.* should be integrated into artificial skin covering a biomimetic robot in order to achieve an auto-feedback function, equivalent or superior to a living organism.[5–8] In order to address this requirement, there have been several reports pertaining to stretchable electronic sensors and electrical wiring embedded into artificial skin.[9–13]

Typically, a certain amount of electrical energy is needed to operate an electronic sensor and transfer the signal to a central processing unit regardless of the type of sensor used (passive or active).[9–11,14–17] When the energy for many sensors is supplied through long and complex electrical wirings from a separate power source, a considerable amount of joule heating, as well as restriction of the sensing area, is unavoidable. One possible solution to this power supply issue can be conceived, which involves a self-powered artificial skin (SPAS) without electrical wirings, where the sensors could be integrated with high densities to mimic closely living skin.[18–20]

Considering the mechanical energy generated from the stretching and bending motions of skin, finding a method for powering the SPAS based on piezoelectric energy harvesting is desirable. Over the past decade, piezoelectric nanogenerator (NG) based self-powered sensing systems have been developed for a variety of sensing applications by several research groups.[21–27] However, no piezoelectric NGs suitable for the SPAS have been designed as of yet, which require a high mechanical stretchability, narrow thicknesses, environmental compatibility, and a large area.

In order to satisfy the requirements for SPAS, we introduce a NG that includes a unique eco-friendly piezoelectric nanomaterial, bi-axially grown (BG) zinc oxide (ZnO) nanorods (NRs), and possesses a large manufacturing area by utilizing a dry rubbing process. There are two essential facets of our design: (1) revealing the mechanism related to the in-plane mode of the

Broader context

A living organism's skin is filled with sensors designed to perceive various external stimuli and to maintain homeostasis by transferring this information to the brain. Recently, various artificial sensors have been integrated into artificial skin covering a biomimetic robot in order to achieve an auto-feedback function, equivalent or superior to a living organism, and there have been several reports related to stretchable electronic sensors and electrical wiring embedded into artificial skin. However, a certain amount of electrical energy is needed to operate an electronic sensor and transfer the signal regardless of the type of sensor used. If the energy is supplied through long and complex electrical wirings from a separate power source, a considerable amount of joule heating, as well as restriction of the sensing area, is unavoidable. A solution of this power supply issue can be conceived, which involves a self-powered artificial skin without electrical wirings, where the sensors could be integrated with high densities to mimic the closely living skin. To satisfy the requirements, we introduce a nanogenerator that includes a unique eco-friendly nanomaterial, bi-axially grown zinc oxide nanorods having an in-plane mode of the piezoelectric action, and possesses a large manufacturing area by a rubbing process.

[a]*Department of BioNano Technology, Gachon University, Seongnam, Korea*
[b]*Department of Materials Science and Engineering, Yonsei University, Seoul, Korea. E-mail: jmmyoung@yonsei.ac.kr*
[c]*Program in Nano Science and Technology, Graduate School of Convergence Science and Technology, Seoul National University, Seoul, Korea*
[d]*Advanced Institutes of Convergence Technology, 864-1 Lui-ong, Yeongtong-gu, Suwon-si, Gyeonggi-do, Korea*
[e]*Schools of Materials Science and Engineering, Georgia Institute of Technology, Atlanta, Georgia, 30332-0245, USA*

† Electronic supplementary information (ESI) available: Experimental section and supplementary figures. See DOI: 10.1039/c4ee02358g

‡ They equally contributed to this work.

piezoelectric action of bent BG ZnO NRs, and (2) assembling a monolayer over a large area by using a rapid rubbing method. Additionally, contrary to previous reports,[21–23,28,29] the designed NG in this work was fabricated without the use of a substrate, and could be utilized as a stretchable, bendable, and on-demand programmable integrated SPAS.

Results and discussion

Fabrication of SPAS

Fig. 1 shows a typical procedure used to manufacture SPAS. The BG ZnO NR powder was prepared using our previously reported hydrothermal method (see the ESI Fig. S1†).[30] A velvet cloth was prepared to adhere to the powder, and polydimethylsiloxane (PDMS) (which was used as a matrix material for SPAS) was deposited on a glass substrate, as shown in Fig. 1a. Fig. 1b shows the one-directional rubbing technique with the velvet cloth on PDMS, which formed a monolayer consisting of BG ZnO NRs aligned with the direction of rubbing within several seconds (see the ESI Video S1†). During the rubbing process, BG ZnO NRs with six non-polar prismatic sides were detached from the velvet cloth and were subsequently affixed to the hydrophobic surface of PDMS according to their in-plane direction, until the entire surface of PDMS was covered with BG ZnO NRs.

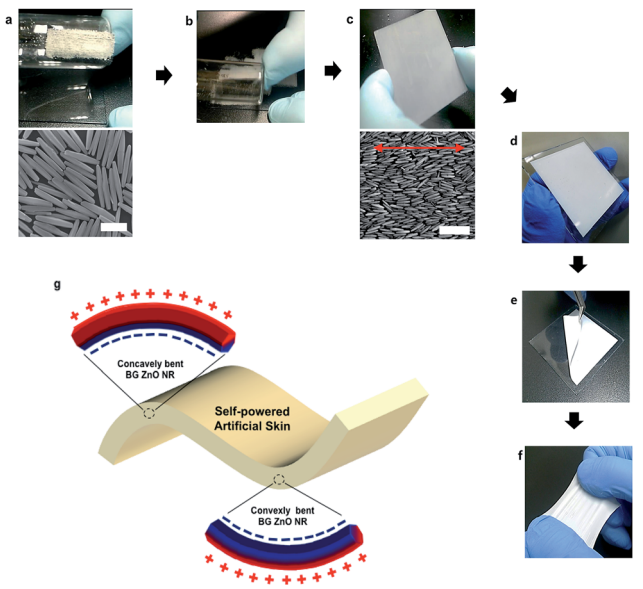

Fig. 1 Self-powered artificial skin (SPAS) fabrication with a bi-axially grown (BG) ZnO NR array on a PDMS film through one-direction rubbing. (a) BG ZnO NR powder on a velvet cloth, which was attached on one side of a round glass tube. The bottom image shows BG ZnO NRs from a hydrothermal synthesis after thermal annealing at 400 °C for 2 h (scale bar = 2 μm). (b) BG ZnO NRs rubbing in one-direction on a PDMS coated slide glass (5 × 5 cm^2). (c) Single monolayer formation of BG ZnO NRs through rubbing. The bottom image indicates a nematic-like array of the BG ZnO NRs (red arrow indicates the rubbing direction; scale bar is 6 μm). (d) Seven layers of the SPAS on a glass substrate. (e) Detachment of the SPAS from the glass substrate. (f) Photograph demonstrating how the SPAS is flexible (in (e)) and stretchable. (g) Schematic 3D diagram describing the piezoelectric potential generation of a bent SPAS.

As a result of the strong Van der Waals forces, the BG ZnO NRs could be stably affixed to PDMS, despite several mechanical sweepings with the velvet cloth. The longitudinal direction of NRs was aligned with respect to the rubbing direction, to minimize the rotational potential energy resulting from the application of one-directional force through the rubbing. An assembled monolayer of BG ZnO NRs on a PDMS-coated glass substrate is shown in Fig. 1c. Finally, after coating another PDMS layer over this monolayer, in order to embed and fasten the BG ZnO NRs into the first PDMS region, a single-layered SPAS was complete.

By repeating this procedure several times, a multi-layered SPAS can be obtained, with a seven-layered SPAS shown in Fig. 1d. The reason for varying the number of BG ZnO NR layers is to modulate the output power in the SPAS, so it can match the amount of electrical energy required for any given application. In order to demonstrate its utility as a stretchable and bendable artificial skin, the SPAS (including the seven monolayers of BG ZnO NRs) was detached from the glass substrate, and its high stretchability was displayed in Fig. 1e and f. We designed the SPAS to be piezoelectrically activated according to the inflection polarity from a mechanical deformation. Thus the bending mode of BG ZnO NRs embedded in PDMS is altered either convexly or concavely, as shown in Fig. 1g. A bent BG ZnO NR receives transverse shear stress–stain and both positive and negative piezoelectrical potentials were generated over the transversal direction.

Piezoelectric behavior of BG ZnO NR

In order to mimic the mechanical deformation of a thin skin on the surface of a living organism, we studied the SPAS when bent over a thick substrate. When the SPAS is bent, the PDMS matrix experiences transverse shear stress–strain, as well as longitudinal tensile or compressive stress–strain, and the laterally placed BG ZnO NRs also experience the same mechanical deformation. Theoretically, the tensile or compressive stress on the *c*-axis of the ZnO NR does not generate piezoelectric polarization along its transversal direction, but instead along the longitudinal direction, as shown in Fig. S2 of the ESI.† Therefore, we did not consider the longitudinal tensile and compressive strains in the SPAS designed to harvest mechanical energy from the piezoelectricity of the BG ZnO NRs along the transversal direction. We only considered the piezoelectric behavior under shear stress–strain along the transversal direction of bent BG ZnO NRs.

We theoretically investigated how the BG ZnO NR (shown in Fig. 2a) transduces the applied mechanical stress into electrical energy. In a bent matrix, each embedded BG ZnO NR aligned to the in-plane direction is symmetrically bent centering on the middle of the NR, so that we could consider the symmetric bending in our theoretical calculations. As shown in Fig. 2b, the BG ZnO NR is assumed to be a cylinder with the following parameters: (1) the diameter and length of the cylinder are 500 nm and 4000 nm, respectively, (2) the *c*-axis parallel to the center-axis (which is parallel (||) to the *z*-axis) of the cylinder is mirror-symmetrically aligned by the *xy*-plane that divides the

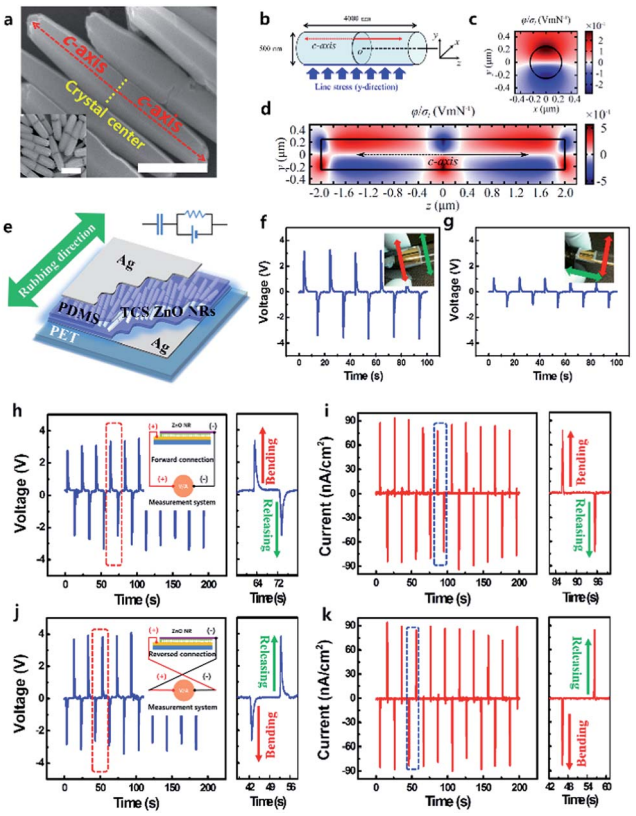

Fig. 2 Mechanism of the piezoelectric potential generation and simulation results of BG ZnO NRs under bending stress. (a) SEM image of the BG ZnO NRs grown for 30 min at 85 °C using a hydrothermal method (scale bar = 1 μm). The red dashed arrow and the yellow dashed line indicate the growth direction (*c*-axis) and crystal center, respectively. The inset shows BG ZnO NRs that were grown for 5 min at 85 °C, and the crystal center is definitely shown (scale bar = 500 nm). (b) Schematic diagram representing the BG ZnO NR. The orientation of the *c*-axis of ZnO in each domain of the cylinder is drawn as a red arrow. The direction of the Cartesian coordinates is also shown, with O denoting the origin on the cylinder-bisecting vertical plane. ((c) and (d)) The piezoelectric potential (φ) corresponding to the BG ZnO cylinder under external line stress (σ_l) which is illustrated as blue schemes in (b). In (d) black arrows and solid lines depict the direction of the *c*-axis and ZnO cylinder boundaries, respectively. (e) Schematic 3D diagram depicting the structure of the SPAS device used to measure the piezoelectric potential. The BG ZnO NRs were placed between PDMS elastic polymer layers. The PET film was used as a supporting substrate to deliver a uniform external bending stress to the active layers. (f) Output voltage of BG ZnO NRs from bending in the same rubbing direction. (g) Output voltage when the device was vertically bent in the rubbing direction. ((h) and (k)) Electrical characteristics from the switching-polarity tests. ((h) and (i)) Output voltage and current density when the device was connected in the forward direction. ((j) and (k)) Output voltage and current density when the device was connected in the reverse direction.

cylinder in half, (3) the mechanical stress and piezoelectricity linearly increase in response to external strains, (4) the matrices of the elastic modulus, piezoelectric coefficients, and relative permittivity of ZnO were taken from the literature,[31] (5) for the ZnO domain where the orientation of the *c*-axis is in the positive (or negative) *z*-direction, the sign of the piezoelectric coefficients is plus (or minus), and (6) the cylinder is surrounded by a dielectric substance with a relative permittivity of 2.3, which is considered to be PDMS.

Fig. 2c and d show the calculated piezoelectric potential distributions in the BG ZnO cylinder, when the mechanical load of the *y*-direction is applied to the line boundary of the cylinder at $y = -250$ nm and $x = 0$ nm. The calculation was performed using the finite element method.[32] The majority of the region at the upper half of the cylinder ($y > 0$) exhibits positively polarized piezoelectric potentials, while displaying the negatively polarized potentials in the lower half. This distribution of polarization is reversed near the cylinder-bisecting *xy*-plane. The net piezoelectric potential of the upper (or lower) half of the cylinder, however, is a meaningful positive (or negative) value, which allows the device to harvest electrical charges at both electrodes. Conversely, a ZnO cylinder, which is unidirectionally grown along the *c*-axis, shows a vastly different piezoelectricity relative to the BG ZnO cylinder. The net potential of the upper (or lower) half of the ZnO cylinder nearly becomes null, as shown in Fig. S3 of the ESI,† when the cylinder is under equal stress. As a result, the notable piezoelectric voltage of the device comes from the uniqueness of the bilaterally oriented *c*-axis of the BG ZnO NR.

In order to verify experimentally our calculated results, a simple piezoelectric energy-harvesting device was fabricated, and its schematic and equivalent circuit diagrams are shown in Fig. 2e. The single-layered SPAS, of which the top and bottom was coated with a silver electrode, was placed on a 1 mm thick polyethylene terephthalate (PET) substrate for the quantitative bending studies, and all devices were operated with a 1 mm bending radius at 0.05 Hz.

When changing the bending direction, different voltage outputs were obtained, as shown in Fig. 2f and g. Only when the BG ZnO NRs are aligned in the bending direction in parallel they can be piezoelectrically activated, based on the above calculations, and the voltage of the parallel bending was three times higher than that of the perpendicular bending. Ideally, not all voltage outputs can be produced through perpendicular bending, however, an output of approximately 1 V was measured, and this value is thought to arise from the imperfect degree of the alignment of BG ZnO NRs in a particular direction.

Additionally, the polarity of the piezoelectric potential produced in the SPAS was determined by a reverse connecting method as shown in Fig. 2h and k. As the device was convexly bent, the positive voltage and current were initially measured at the top electrode, as shown in Fig. 2h and i. This result coincided perfectly with the calculated prediction. When the electrical connecting direction was reversed, the polarities of the voltage and current at the top electrode were measured to be negative, as shown in Fig. 2j and k. Therefore, we were able to prove that the electrical energy output from the bent SPAS originates from piezoelectrically activated BG ZnO NRs, which were assembled with an in-plane monolayer.

Power modulating strategies

Modulation of the output power is an important characteristic of the SPAS, in order to match the required power in a sensor.

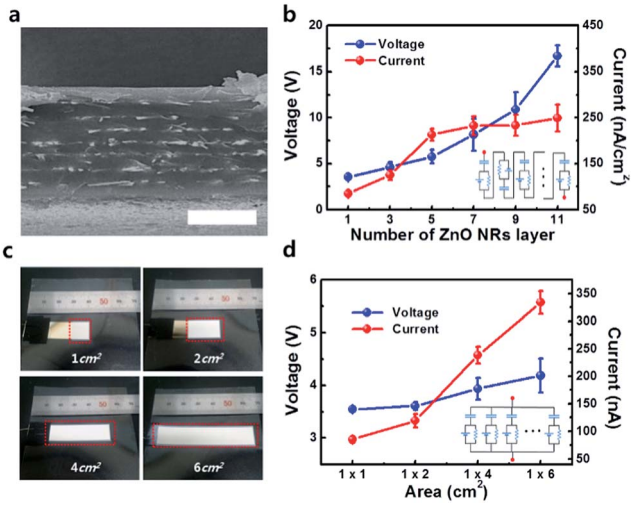

Fig. 3 Power modulation in SPAS; series or parallel connections. (a) Cross sectional SEM image of a seven BG ZnO NR layered SPAS (scale bar = 20 μm). (b) Summarization of the output voltage and current as the number of BG ZnO NR layers increased. The inset schematic describes an equivalent circuit diagram with a multi-stacked configuration. (c) Bird's eye view of various areas of the SPAS, from 1 to 6 cm^2. (d) Summarization of the output voltage and current as the area of SPAS increases. The inset schematic describes an equivalent circuit diagram with a parallel connection.

One strategy to modulate the power of the SPAS is to stack piezoelectric BG ZnO NR monolayers in a series (Fig. 3a), where the seven monolayers of the BG ZnO NR that were inserted into the PDMS layers are clearly observed. Fig. 3b shows the output voltage and current increasing with additional layers of the BG ZnO NR monolayer. Considering the equivalent circuit of the series connection, shown in the inset of Fig. 3b, the tendency of the output voltage was reasonable, but the output current was abnormal, judged by its resultant capacitance. The linear accumulation of the piezoelectric potential was represented by a linearly increasing output voltage with respect to the amount of stacked BG ZnO NR monolayers. However, the output current cannot theoretically be increased by the multi-stacking of the piezoelectric active layer in series, since the accumulated charge density on each active layer should be kept constant. In our investigation, the reason for increasing the output current is the increase of shear strain caused by the excessive downward shifting of the neutral line of bending proportionally with the amount of stacks present. As the number of stacks increased, the output current gradually saturated, as shown in Fig. 3b. If additional stacking piezoelectric layers were introduced, the current would decrease. The output power deterioration of our SPAS in the example of excessive downward shifting of the neutral line of bending was systematically demonstrated in the ESI Fig. S4.†

Another strategy to modulate the power in the SPAS is to enlarge the active area of piezoelectric BG ZnO NR monolayers in parallel, as shown in Fig. 3c, where the bent area linearly increased from 1 to 6 cm^2. Fig. 3d shows that the output current was proportional to the area of the BG ZnO NR monolayer, whereas the output voltages were nearly unchanged. Considering total capacitance based on the equivalent circuit of the parallel connection (shown in the inset of Fig. 3d), the tendencies of the output current and voltage were reasonable.

Programmable integration

To highlight there results, the programmable integration of twelve pieces of SPAS was demonstrated to achieve the output voltage and current on-demand, as shown in Fig. 4. A single-layer SPAS was fabricated on a glass substrate, and a silver electrode was then deposited on it, as shown in Fig. 4a. By simply cutting the material, this layer was split into seventy-two pieces of SPAS, with each piece possessing an area of 16 mm^2, and was subsequently detached for programmable integration, as shown in Fig. 4b. On the previously designed bottom electrodes, each piece of SPAS was integrated in to a 3 × 4 array,

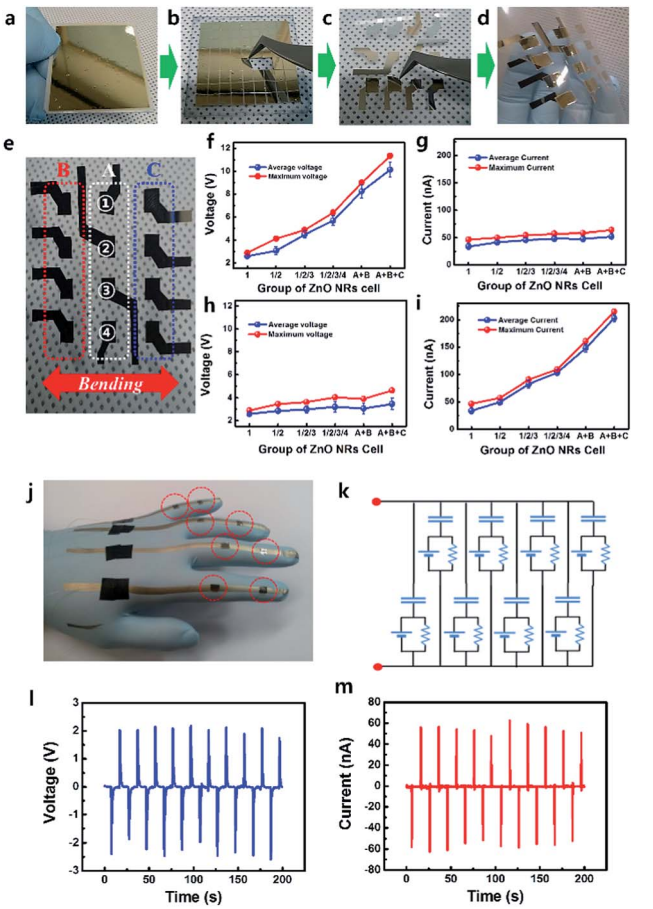

Fig. 4 Programmable integration of SPAS. (a–d) A sequential procedure describing the programmable integration of SPAS on pre-designed electrode patterns. (e) 3 × 4 array of twelve SPASs with the columns and rows being marked by B, A, C, and 1, 2, 3, 4, respectively. (f and g) Output voltage and current for the series combination of SPASs. (h and i) Output voltages and currents for the parallel combinations of SPASs. (j) A photograph of a gloved human hand with eight SPASs integrated on bent sites. (k) An equivalent circuit diagram of the eight SPASs connected in parallel on the gloved human hand. (l and m) Output voltage and current of the eight SPASs experiencing the motion of grasping and unfolding the hand.

which was completed after soldering silver wires to measure the output power, as shown in Fig. 4c and d. Fig. 4e shows three columns marked A, B, and C, and four rows marked 1, 2, 3, and 4. The bending test was performed along the direction of the rows.

For the series connection with each piece of SPAS, the output voltage could be modulated by approximately 0.63 V per additional piece of SPAS (16 mm^2), while the current was maintained, as shown in Fig. 4f and g. Alternatively, the output current in the parallel connection could be modulated by approximately 33 nA per additional piece of SPAS (16 mm^2), while the voltage was maintained, as shown in Fig. 4h and i. If we combine the n series and the $(12 - n)$ parallel connections, $\{50 + 33 \times (n - 1)\}$ nA with $\{2.5 + 0.63 \times (11 - n)\}$ V can be generated. There are twelve possible combinations of current and voltage. Additionally, the area of a piece of SPAS can be a varied in order to modulate the output power further. Therefore, a certain voltage and current required for a sensor can be satisfied with our programmable integration of the SPAS sample.

Finally, to demonstrate the practical application of the SPAS on living skin, eight pieces of SPAS were integrated on the convexly bent positions of four human fingers wearing a nitrile rubber glove, upon which bottom electrodes were prepared, as shown in Fig. 4j, and its equivalent circuit diagram is illustrated in Fig. 4k. After soldering silver wires at each position, the output voltage and current were measured while repeatedly clenching and opening the fist (see the ESI Video S2†). The resulting output voltage and current are shown in Fig. 4l and m, and values of 2 V and 60 nA were produced from the bending motion of the fingers.

Conclusions

In conclusion, SPAS containing a large area of BG ZnO NRs, fabricated using a rapid dry rubbing process, was introduced as a power source for sensors embedded in artificial skin. The mechanism related to the in-plane mode of the piezoelectric action of a bent BG ZnO NR was investigated by a theoretical calculation, and verified through various experimental measurements of the output current and voltage from a piece of SPAS in a convexly bending environment. Additionally, strategies for the modulation of the output power of our SPAS were demonstrated, which could be achieved through multi-stacking or enlarging the area of the SPAS. As a highlight of this communication, on-demand programmable integrations in series and parallel with several pieces of SPAS were demonstrated on twelve convexly bent positions on a plastic substrate, and on eight separate positions on four human fingers wearing a rubber glove. The output voltage and current from these arrays of SPASs were then successfully observed.

Although our SPAS material is a small step in the advancement of future artificial skin technology, it deserves recognition as a promising approach towards the first mechanically driven self-powered system embedded in artificial skin. In addition to providing an energy source for various self-powered sensors integrated in artificial skin, when a biocompatible matrix instead of PDMS is used, our SPAS can supply the electrical energy for implanted biomedical devices from the mechanical bending motion.

Acknowledgements

This research was supported by the WCU (World Class University) program (R32-20031) funded by the Ministry of Education of Korea and by the Center for Advanced Soft-Electronics (2013M3A6A5073177) as Global Frontier Project funded by the Ministry of Science, ICT and Future Planning of Korea. This research was also supported by Grant Nos. 2010-0029207 from the National Research Foundation (NRF) which is funded by the Korean government (MEST) and by the LG Display academic industrial cooperation program.

Notes and references

1 M. Corbetta and G. L. Shulman, *Nature*, 2002, **3**, 201.
2 R. A. Poldrack, J. Clark, E. J. Pare-Blagoev, D. Shoharmy, J. Creso Moyano, C. Myers and M. A. Gluck, *Nature*, 2001, **414**, 546.
3 D. S. Bassett and E. T. Bullmore, *Curr. Opin. Neurol.*, 2009, **22**, 340.
4 M. A. Arbib, *The Handbook of Brain Theory and Neutral Networks*, MIT Press, Cambridge Mass, 2nd edn, 2002.
5 L. Robertsson, B. Iliev, R. Palm and P. Wide, *Int. J. Man-Mach. Stud.*, 2007, **65**, 446.
6 B. Webb, *Nature*, 2002, **417**, 359.
7 K.-J. Cho, J.-S. Koh, S. Kim, W.-S. Chu, Y. Hong and S.-H. Ahn, *Int J. Precis. Eng. Manuf.*, 2009, **10**, 171.
8 T. Someya, T. Sekitani, S. Iba, Y. Kato, H. Kawaguchi and T. Sakurai, *Proc. Natl. Acad. Sci. U. S. A.*, 2004, **101**, 9966.
9 D. J. Lipomi, M. Vosgueritchian, B. C.-K. Tee, S. L. Hellstrom, J. A. Lee, C. H. Fox and Z. Bao, *Nat. Nanotechnol.*, 2011, **6**, 788.
10 M. Ramuz, C.-K. Benjamin, J. Tee, B.-H. Tok and Z. Bao, *Adv. Mater.*, 2012, **24**, 3223.
11 T. Someya, Y. Kato, T. Sekitani, S. Iba, Y. Noguchi, Y. Murase, H. Kawaguchi and T. Sakurai, *Proc. Natl. Acad. Sci. U. S. A.*, 2005, **102**, 12321.
12 J. A. Rogers, T. Someya and Y. Huang, *Science*, 2010, **327**, 1603.
13 T. Sekitani, Y. Noguchi, K. Hata, T. Fukushima, T. Aida and T. Someya, *Science*, 2008, **321**, 1468.
14 T. Tamada, Y. Hayamizu, Y. Yamamoto, Y. Yomogida, A. Izadi-Najafabadi, D. N. Futaba and K. Hata, *Nat. Nanotechnol.*, 2011, **6**, 296.
15 S. Lai, M. Demelas, G. Casula, P. Cosseddu, M. Barbaro and A. Bonfiglio, *Adv. Mater.*, 2013, **25**, 103.
16 T. S. Sreeprasad, A. A. Rodriguez, J. Colston, A. Graham, E. Shishkin, V. Pallem and V. Berry, *Nano Lett.*, 2013, **13**, 1757.
17 F. K. Perkins, A. L. Friedman, E. Cobas, P. M. Campbell, G. G. Jernigan and B. T. Jonker, *Nano Lett.*, 2013, **13**, 668.
18 Z. L. Wang and J. Song, *Science*, 2006, **312**, 242.
19 W. Wu, X. Wen and Z. L. Wang, *Science*, 2013, **340**, 952.

20 S. Y. Chung, S. Kim, J. Lee, K. Kim, S. Kim, C. Kang and Y. S. Kim, *Adv. Mater.*, 2012, **24**, 6022.
21 S. Xu, Y. Qin, C. Xu, Y. Wei, R. Yang and Z. L. Wang, *Nat. Nanotechnol.*, 2010, **5**, 366.
22 Y. Hu, J. Zhou, P.-H. Yeh, Z. Li, T.-Y. Wei and Z. L. Wang, *Adv. Mater.*, 2010, **22**, 3327.
23 R. Yu, C. Pan and Z. L. Wang, *Energy Environ. Sci.*, 2013, **6**, 494.
24 H.-K. Park, K. Y. Lee, J.-S. Seo, J.-A. Jeong, H.-Ki. Kim, D. Choi and S.-W. Kim, *Adv. Funct. Mater.*, 2011, **21**, 1187.
25 J.-H. Lee, K. Y. Lee, B. Kumar, N. T. Tien, N.-E. Lee and S.-W. Kim, *Energy Environ. Sci.*, 2013, **6**, 169.
26 K.-I. Park, M. Lee, Y. Liu, S. Moon, G.-T. Hwang, G. Zhu, J. E. Kim, S. O. Kim, D. K. Kim, Z. L. Wang and K. J. Lee, *Adv. Mater.*, 2012, **24**, 2999.
27 K.-I. Park, S. Xu, Y. Liu, G.-T. Hwang, S. Joong, L. Kang, Z. L. Wang and K. J. Lee, *Nano Lett.*, 2010, **10**, 4939.
28 Y. S. Zhou, K. Wang, W. Han, S. C. Rai, Y. Zhang, Y. Ding, C. Pan, F. Zhang, W. Zhou and Z. L. Wang, *ACS Nano*, 2012, **6**, 6478.
29 S. Lee, J.-I. Hong, C. Xu, M. Lee, D. Kim, L. Lin, W. Hwang and Z. L. Wang, *Adv. Mater.*, 2012, **24**, 4398.
30 W. S. Jang, T. I. Lee, J. Y. Oh, S. H. Hwang, S. W. Shon, D. H. Kim, Y. Xia, J. M. Myoung and H. K. Baik, *J. Mater. Chem.*, 2012, **22**, 20719.
31 Y. Gao and Z. L. Wang, *Nano Lett.*, 2007, **7**, 2499.
32 COMSOL Multiphysics®, http://www.comsol.com.

